Comparative Transient Stability Assessment of Droop and Dispatchable Virtual Oscillator Controlled Grid-Connected Inverters

Hui Yu, *Student Member, IEEE*, M. A. Awal, *Student Member, IEEE*, Hao Tu, *Student Member, IEEE*, Iqbal Husain, *Fellow, IEEE*, and Srdjan Lukic, *Senior Member, IEEE*

***Abstract*—With the increasing integration of power electronics interfaced distributed generators, transient stability assessment of grid-connected inverters subjected to large grid disturbances is of vital importance for the secure and resilient operation of the power grid. Dispatchable virtual oscillator control (dVOC) is an emerging approach to implement nonlinear control of grid-forming inverters. Through coordinate transformation, a simple first-order nonlinear power angle dynamic equation is uncovered from the complex oscillator dynamics. Furthermore, this article proposes a concise and straightforward graphical approach to assess transient stability of dVOC using vector field on the circle. To provide a more in-depth analysis, a complete large-signal model is derived and the impact of dVOC voltage amplitude dynamics is analyzed. For comparison, transient stability of the currently prevalent droop control is also assessed using phase portraits. Salient transient stability features of dVOC and droop control during grid faults are summarized and compared. The theoretical analysis is validated by controller hardware-in-the-loop testbed using industry-grade hardware.**

***Index Terms*—Dispatchable virtual oscillator control (dVOC), droop control, grid forming, phase portrait, transient stability, vector field on the circle.**

I. Introduction

In ac microgrids, grid-forming inverter is an essential component that can operate in both islanded and grid-connected modes. Droop control is the prevalent primary control method for grid-forming inverters, which has been widely adopted in ac microgrids [1], [2]. In islanded mode, droop control allows decentralized power sharing between paralleled inverters by introducing frequency and voltage deviations from nominal values. In grid-connected mode, droop control allows remote power dispatch of available resources throughout the grid. Virtual synchronous machine (VSM) is a popular variation of droop control with an emphasis on inertia emulation [3], [4]. Under the primary control, voltage tracking control is required and usually achieved by a dual loop control structure [2]. To allow proper operation of the hierarchical control structure, a clear timescale separation between the primary and voltage control has to be guaranteed [1], [4]–[6]. In practice, low-pass filters (LPFs) are indispensable for droop control implementation to suppress the power fluctuations and stabilize the system [7], [8].

Virtual oscillator control (VOC) [9]–[17] is an emerging grid-forming control technique for ac microgrid inverters. The basic idea of VOC is to control the inverters to mimic the dynamics of weakly nonlinear limit-cycle oscillators, such as dead-zone oscillator [10], [11] and Van der Pol oscillator [12], [13], [18]. Benefiting from the synchronization characteristic of coupled oscillators network, a VOC-based inverter network (i.e., ac microgrid) can synchronize in a communicationless fashion [9]–[11]. One salient feature of VOC is its capability to rapidly stabilize the oscillator to a limit cycle, i.e., reach the sinusoidal steady state of the inverter output voltage from any initial condition [9]–[13]. Therefore, VOC achieves global asymptotic synchronization and better transient performance than the traditional droop control [17]. In comparison, droop control is a phasor domain controller, which is well defined only near the synchronous speed [5], [13] and is only locally exponentially stable [19]. Furthermore, VOC combines the voltage control with primary control. Unlike droop control, VOC does not need control layer separation, power calculation, and LPFs, which make VOC much faster in terms of synchronization speed and power sharing [5], [13].

Recently, an improved VOC implementation based on Hopf type oscillator was proposed in [20]–[23]. It is termed dispatchable VOC (dVOC) due to the fact that it allows setpoint dispatch, whereas existing VOC requires complex structure to achieve the same objective [15], [16]. Moreover, dVOC has smaller harmonic distortions and is preferable to VOC for three-phase applications [23], [24].

Among the many issues for grid-forming inverters, stability is one of the most important. While a majority of the research works focus on small-signal stability, little effort has been devoted to the transient stability analysis. Similar to its definition in traditional power systems, transient stability in this article

Manuscript received November 18, 2019; revised March 2, 2020 and May 6, 2020; accepted June 28, 2020. Date of publication July 7, 2020; date of current version September 22, 2020. This work was supported by the National Science Foundation under Award EEC-0812121 for the FREEDM Engineering Research Center. Recommended for publication by Associate Editor X. Wang. *(Corresponding author: Hui Yu.)*

The authors are with the Future Renewable Electric Energy Delivery and Management Systems Center, North Carolina State University, Raleigh, NC 27695 USA (e-mail: hyu11@ncsu.edu; mawal@ncsu.edu; htu@ncsu.edu; ihusain2@ncsu.edu; smlukic@ncsu.edu).

Color versions of one or more of the figures in this article are available online at https://ieeexplore.ieee.org.

Digital Object Identifier 10.1109/TPEL.2020.3007628

refers to the ability of the grid-forming inverter to maintain synchronism with the utility grid when subjected to a large transient disturbance, such as transmission line faults (e.g., out of service, three-phase short-circuit fault), loss of a large load, and severe grid voltage sags [25].

For droop control, various research works on transient stability have been reported recently. Transient stability analysis for VSM was proposed in [26] and [27] using equal area criterion (EAC) based on power–angle ($P-\delta$) curve, which is widely used in the transient stability study of conventional power systems. EAC is applicable to VSM since it has a similar second-order swing equation to synchronous machines [4]. In [28], a Lyapunov function based method was used to evaluate the transient stability of VSM. Recently in [29], a mode-adaptive power angle control method is proposed for transient stability enhancement of VSM. Transient stability analysis for power synchronization control (PSC) reveals a first-order nonlinear power angle dynamic equation [30], [31]. By using the phase portrait method ($\dot{\delta}-\delta$ curve), it is found that the PSC-based inverter will maintain synchronization with the grid as long as there are equilibrium points. Moreover, the inverter can still resynchronize with the grid after around one cycle of oscillation even with delayed fault clearance. In [32]–[34], the influence of the overcurrent limit on transient stability was analyzed. Under extreme fault cases, the current limit of the inverter is reached and the inverter controller will transition to phase-locked loop (PLL) synchronized current control [31], [35]. Under these extreme fault conditions, the transient stability characteristics will be largely determined by the PLL, which has been well-addressed in [36] and [37] and will not be discussed in this article.

Recently, the coupling effect between the active and reactive power control loops for droop-controlled converters was studied in [38]–[40]. When a large grid disturbance occurs, the inverter output voltage might be regulated at a considerably low value to maintain the reactive power control, which deteriorates the transient stability. Phase portrait analysis based on $\dot{\delta}-\delta$ and $V-\delta$ curves demonstrates that proper design of the LPF in the reactive power control loop can alleviate the instability issues. Conversely, alternating voltage control (AVC) mode is suggested to provide the best possible voltage support in weak grid conditions by keeping the inverter terminal voltage constant (thus not explicitly controlling the reactive power) [31], [35].

In this article, we propose a comprehensive transient stability assessment method for dVOC-based inverter network. Although the superior transient performance has been demonstrated for dVOC-based islanded microgrids, the transient stability of dVOC-based grid-connected inverter when subjected to severe transient disturbance has not been investigated in the literature. The lack of an effective and simple tool for the transient stability analysis of dVOC under large grid disturbances will greatly restrict the adoption of this novel control algorithm in practical applications. In this article, we present a first-order nonlinear power angle dynamic equation derived from the oscillator dynamics, which is shown to be a nonuniform oscillator. Vector field on the circle, a graphical method for analysis of first-order nonlinear systems with possible periodic solutions [41], is adopted to analyze the stability of the nonuniform oscillator model. Compared to the phase portrait method proposed in [31] that analyzes first-order nonlinear dynamics on the line, the vector field on the circle method provides a clearer and more straightforward interpretation of first-order nonlinear systems that exhibit oscillatory response [41]. Salient transient stability features of dVOC under different fault conditions and fault-clearing schemes are analyzed. It is found that dVOC outperforms droop control in terms of transient stability when subjected to large grid disturbances. Furthermore, a complete large-signal model for dVOC-based grid-connected inverters considering the coupling effect of active and reactive power is developed. Based on this model, an in-depth analysis on the impact of the voltage amplitude dynamics on transient stability of dVOC by using $\dot{\delta}-\delta$ and $V-\delta$ curves is carried out. The analysis provides a new perspective for designing dVOC by recognizing the effect of parameters selection on the transient stability [23].

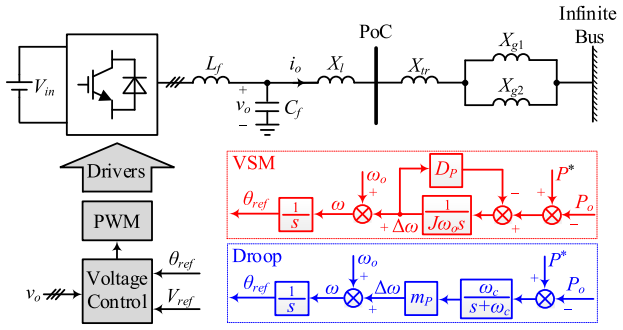

Fig. 1. Diagram of grid-connected inverters with droop control or VSM.

The rest of this article is organized as follows. In Section II, transient stability of droop control is assessed by using phase portrait. In Section III, the dVOC power angle dynamic equation is derived. In Section IV, the transient stability of dVOC is analyzed using vector field on the circle. In Section V, the impact of the voltage dynamics on the transient stability of dVOC is analyzed. In Section VI, the theoretical analysis is validated using an OPAL-RT-based real-time controller hardware-in-the-loop (C-HIL) testbed. Finally, Section VII concludes this article.

II. Transient Stability Analysis of Droop Control

To study the transient stability of droop control and dVOC, we adopt a standard setup for transient stability analysis in power systems [25], [31], [40], as shown in Fig. 1. The system consists of a three-phase inverter connected to an infinite bus through two parallel transmission lines. The line impedances are assumed to be dominantly inductive; grid faults do not trigger the overcurrent limit are only of interest; and the inverter is assumed to be operating in AVC mode. In addition, the fast voltage loop dynamics are ignored.

As shown in Fig. 1, for droop control, LPF is used to eliminate rapid power fluctuations and measurement noise [7], [8] and can also be designed for inertia emulation [39]. Droop control and VSM are mathematically equivalent with the following

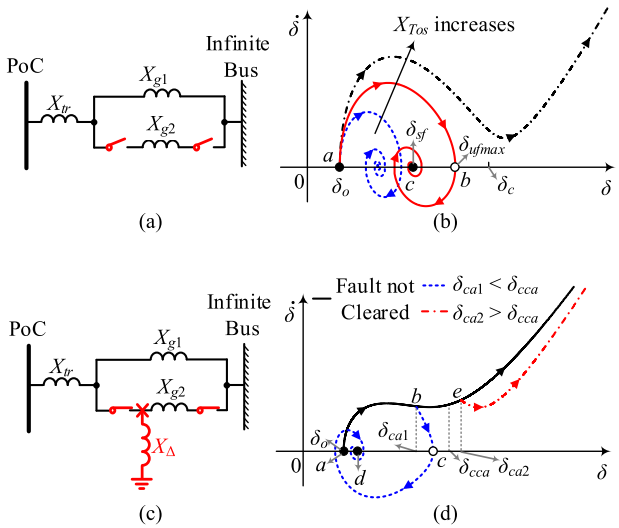

Fig. 2. Transient stability analysis of droop control using phase portraits. (a) Out-of-service fault. (b) Out-of-service fault response. (c) Short-circuit fault. (d) Short-circuit fault response.

relationships [7]:

$$J\omega_o = \frac{1}{\omega_c m_P}, \quad D_P = \frac{1}{m_P} \tag{1}$$

where ω_o is the nominal frequency, m_P is the droop control gain, and J and D_P denote the VSM moment of inertia and damping factor, respectively. By defining the power angle δ as the phase difference between the inverter and infinite bus, its dynamic equation is directly given as [40]

$$\ddot{\delta} + \omega_c \dot{\delta} = \omega_c m_p (P^* - P_o) \tag{2}$$

where P_o and P^* are the inverter output active power and its reference, respectively. The power from the inverter to the infinite bus is given by

$$P_o = P_{\max} \sin\delta, \quad P_{\max} = \frac{3V_o V_g}{X_T} \tag{3}$$

where V_o and V_g are the inverter output voltage and grid voltage (rms), respectively; $P_{\max}$ is the theoretical maximum power the inverter can deliver to the infinite bus; and X_T is the total reactance between the inverter and the infinite bus. Equilibrium point, which refers to the condition that $P^* = P_o$, is said to exist if $P^* < P_{\max}$ [31], [40]. It should be noted that in this article, equilibrium point is different from the fixed point in the phase portrait, which refers to any operating point that satisfies $\dot{\delta} = 0$. Next, two typical fault cases depending on whether equilibrium point exists during the disturbance are illustrated. The parameters of the droop controller used in the study are provided in Table I in Section VI.

A. Case 1: Equilibrium Point Exists During Fault

The out-of-service fault is shown in Fig. 2(a), where the circuit breakers on both sides of the second transmission line are open. The total reactance increases and is given as

$$X_{Tos} = X_l + X_{tr} + X_{g1}. \tag{4}$$

Fig. 2(b) shows the corresponding phase portraits of the system for different X_{Tos} values.

Referring to Fig. 2(b), initially, the system is at point a. After disturbance, the power angle evolves in different ways for different values of X_{Tos}. In the red solid line case, δ first increases to point b, which is an open circle representing an unstable fixed point. The system trajectory moves away until it reaches a stable fixed point c, which is marked by a solid black dot. There are a number of unstable fixed points along the trajectory that are not marked in this figure for clarity. The power angle of the maximum unstable and stable fixed points are denoted as δ_{ufmax} and δ_{sf}, respectively. Before the system finally reaches δ_{sf}, back and forth oscillations exist in the power angle response. As can be seen in Fig. 2(b), δ_{ufmax} will increase as X_{Tos} increases. If δ_{ufmax} crosses over a critical point δ_c, no fixed point exists, leading to loss of synchronism.

B. Case 2: No Equilibrium Point During Fault

The three-phase to ground short-circuit fault is shown in Fig. 2(c). The total reactance increases considerably, which may even result in no equilibrium point ($P^* > P_{\max}$)

$$X_{Tsc} = X_l + X_{tr} + \frac{X_{g1}X_{g2}}{X_{g1}+X_{g2}} + \frac{(X_l + X_{tr})X_{g1}X_{g2}}{(X_{g1}+X_{g2})X_\Delta} \tag{5}$$

where X_Δ denotes the grounding reactance. To avoid system collapse, the fault is then cleared by isolating the second transmission line. Based on different fault-clearing schemes, the phase portraits will be different, as shown in Fig. 2(d).

Initially, the system is at point a. After disturbance, δ keeps increasing and finally leads to loss of synchronism. If the fault is cleared earlier at point b with a fault-clearing angle of δ_{ca1}, first, the phase portrait reaches an unstable fixed point c and finally settles down to a stable fixed point d through multiple oscillations. However, if the fault-clearing angle is large, such as that at point e (δ_{ca2}), the phase portrait does not have any fixed points and δ approaches infinity. The critical-clearing angle (CCA) δ_{cca} is defined by the control parameters and system parameters.

The transient stability features of droop control can be summarized as follows.

1) The system may lose synchronism even if an equilibrium point exists ($P^* < P_{\max}$) after disturbance.
2) If the inverter can reach stable operation after disturbance, overshoots and oscillations always exist in the power angle transient response.
3) If the fault is cleared before CCA, the system can be stable; otherwise, synchronism is lost. Besides, the CCA is determined by both system and control parameters, which complicates the protection system design.

III. Derivation of dVOC Power Angle Dynamics

In this article, a Hopf-type oscillator is adopted due to its perfectly circular limit cycle, improved dynamic performance, and power setpoint dispatch capability. The parameter design

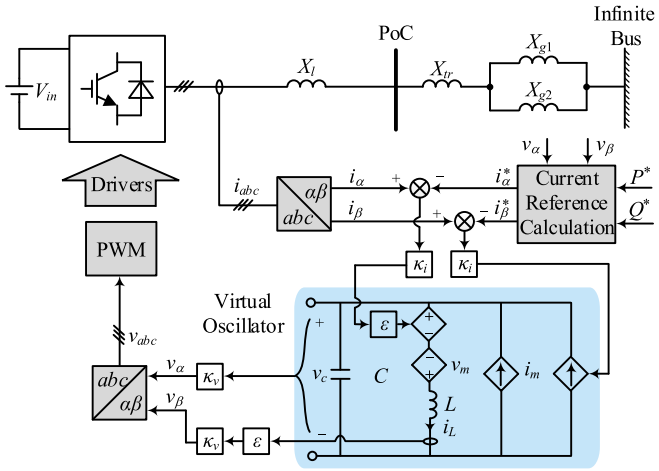

Fig. 3. Control system diagram of dVOC.

guidelines of dVOC can be found in [20], [21], [23]. A very brief description of dVOC is provided in the following.

The control diagram of dVOC is provided in Fig. 3. The virtual oscillator in Fig. 3 is a circuit representation of the Hopf oscillator, which is implemented in a digital processor. The oscillator consists of an LC tank with a resonant frequency of $\omega_o = 1/\sqrt{LC}$, where the capacitor voltage and scaled inductor current are defined as the state variables: $\boldsymbol{x}_{\text{osc}} = [v_c, \varepsilon i_L]^T$, and $\varepsilon = \sqrt{L/C}$. The nonlinear part of the circuit is defined by the dependent voltage source v_m and current source i_m

$$v_m = \frac{\xi}{\omega_o}\left(2X_{\text{nom}}^2 - ||\boldsymbol{x}_{\text{osc}}||\right)\varepsilon i_L \tag{6}$$

$$i_m = \frac{\xi}{\varepsilon\omega_o}\left(2X_{\text{nom}}^2 - ||\boldsymbol{x}_{\text{osc}}||\right)v_c \tag{7}$$

where $||\cdot||$ denotes the Euclidean norm, $\sqrt{2}X_{\text{nom}}$ is the radius of the circular limit cycle of the Hopf oscillator, and ξ is a design parameter that controls the convergence speed of the oscillator. The oscillator is excited by two inputs that determine the dynamics and the steady-state droop response of the oscillator [23], [42]. In this article, $P-\omega$ and $Q-V$ droop relation is chosen for dVOC to match the design of the droop controller in Fig. 1. For this purpose, the α-axis and β-axis current error signals are scaled by κ_i and sent to the oscillator. The current references i^*_α and i^*_β are obtained based on instantaneous power theory. For specific active and reactive power references P^* and Q^*, the current reference is calculated as

$$\begin{bmatrix} i^*_\alpha \\ i^*_\beta \end{bmatrix} = \frac{2}{3(v_\alpha^2 + v_\beta^2)}\begin{bmatrix} v_\alpha & v_\beta \\ v_\beta & -v_\alpha \end{bmatrix}\begin{bmatrix} P^* \\ Q^* \end{bmatrix}. \tag{8}$$

It should be noted that unlike droop control, dVOC does not require power measurement or calculation during operation. Finally, to interface the oscillator with the inverter power stage, the two oscillator states are scaled and sent to the power stage as the modulation signal to generate pulsewidth modulation (PWM) signals

$$\boldsymbol{v}_{\alpha\beta} = [v_\alpha, v_\beta]^T = \kappa_v \boldsymbol{x}_{\text{osc}}. \tag{9}$$

Based on the aforementioned definitions, the dynamic equations for the dVOC are given as

$$\dot{v}_\alpha = \frac{\xi}{\kappa_v^2}\left(2\,V_{\text{nom}}^2 - ||\boldsymbol{v}_{\alpha\beta}||^2\right)v_\alpha - \omega_o v_\beta + \frac{\kappa_v\kappa_i}{C}(i_\beta - i^*_\beta) \tag{10}$$

$$\dot{v}_\beta = \frac{\xi}{\kappa_v^2}\left(2\,V_{\text{nom}}^2 - ||\boldsymbol{v}_{\alpha\beta}||^2\right)v_\beta + \omega_o v_\alpha - \frac{\kappa_v\kappa_i}{C}(i_\alpha - i^*_\alpha) \tag{11}$$

where $V_{\text{nom}} = \kappa_v X_{\text{nom}}$ is the nominal line-to-neutral output voltage (rms).

To uncover the instantaneous voltage amplitude and phase dynamics, the model can be transformed to polar coordinates

$$\sqrt{2}V = ||\boldsymbol{v}_{\alpha\beta}||, \quad \theta = \arctan(v_\beta/v_\alpha) \tag{12}$$

where V and θ are the instantaneous rms voltage amplitude and phase angle, respectively. In the polar coordinates, the dynamics in (10) and (11) are obtained as the following nonlinear differential equations:

$$\dot{V} = \frac{\xi}{\kappa_v^2}V\left(2\,V_{\text{nom}}^2 - 2\,V^2\right) - \frac{\kappa_v\kappa_i}{3CV}\left(Q_o - Q^*\right) \tag{13}$$

$$\dot{\theta} = \omega_o - \frac{\kappa_v\kappa_i}{3CV^2}\left(P_o - P^*\right) \tag{14}$$

where P_o an Q_o are the instantaneous inverter output active and reactive power derived via instantaneous power theory. Compared to the complicated instantaneous voltage dynamics presented in (10) and (11), (13) and (14) show the relationship between $P_o - \omega$ and $Q_o - V$, respectively, and elucidate the relationship between the instantaneous power and voltage and phase dynamics. $P_o - \omega$ and $Q_o - V$ relationships in dVOC resemble droop control, but they are more complex with nonlinearity caused by the voltage amplitude dynamics.

Similar to droop control, the power angle in dVOC is defined as the phase difference between the oscillator and the infinite bus, i.e., $\delta = \theta - \theta_g$. The infinite bus is assumed to be operating at a frequency of ω_o, i.e., $\dot{\theta}_g = \omega_o$. Substituting $\theta = \delta + \theta_g$ in (14) the dVOC power angle dynamics can be derived as

$$\dot{\delta} = -\frac{\kappa_v\kappa_i}{3CV^2}\left(P_o - P^*\right). \tag{15}$$

With dVOC, the power flow equation in (3) is still applicable. Substituting (3) into (15)

$$\dot{\delta} = \frac{\kappa_v\kappa_i}{3CV^2}\left(P^* - \frac{3VV_g}{X_T}\sin\delta\right). \tag{16}$$

The dVOC power angle dynamic equation given by (16) is a first-order nonlinear differential equation, which is fundamentally different from that of droop control given by (2). In (2), the inverter terminal voltage is considered as a constant value by assuming that the inverter is under AVC mode. The AVC mode is preferable in weak grid conditions to provide the best possible voltage support [31], [35]; this is further validated from a transient stability perspective in [38] and [40]. In a weak grid scenario, the reactive power control loop can severely deteriorate the transient stability of the system. Due to its limit-cycle nature,

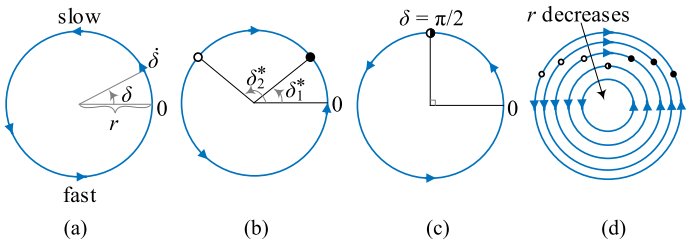

Fig. 4. Vector field of the power angle of grid-connected dVOC on the circle. (a) $r < \omega_r$. (b) $r > \omega_r$. (c) $r = \omega_r$. (d) Fixed ω_r.

dVOC can easily achieve very narrow range of voltage regulation [12], [20]. Hence, for dVOC, the voltage has a negligible influence on the transient stability. Nevertheless, unlike the droop controller in AVC mode, dVOC cannot provide perfect voltage regulation. The voltage amplitude dynamics impact on dVOC transient stability will be discussed in Section V. In the next section, the transient stability of dVOC is assessed based on the assumption that it is appropriately designed for weak grid operation and its voltage amplitude is quasi-constant.

IV. Transient Stability Assessment of dVOC Without Consideration of Voltage Amplitude Dynamics

In this section, we utilize vector field on the circle approach to analyze the power angle dynamic equation of dVOC and assess the controller's transient stability. Compared to phase portrait method, which analyzes first-order nonlinear dynamics on the line, the vector field on the circle method provides a much clearer and more straightforward interpretation of first-order nonlinear system dynamics, such as the power angle dynamics of dVOC, that exhibit an oscillatory response [41].

A. Graphical Assessment Based on Vector Field

For ease of analysis, the following definitions are introduced:

$$\omega_r := \frac{\kappa_v \kappa_i}{3CV^2} P^* \tag{17}$$

$$r := \frac{\kappa_v \kappa_i V_g}{C V X_T} \tag{18}$$

where $\omega_r > 0$ and $r > 0$. Assuming that the dVOC voltage amplitude is constant, ω_r will also be a constant value.

The power angle dynamic equation in (16) is rewritten as

$$\dot{\delta} = f(\delta) := \omega_r - r \sin \delta. \tag{19}$$

Equation (19) describes a nonuniform oscillator that is very common in science and engineering [41]. In (19), $f(\delta)$ is a real valued, 2π-periodic function. The vector field on the circle can be readily plotted for $\dot{\delta} = f(\delta)$, where δ is a point on the circle and $\dot{\delta}$ is the velocity vector at that point, as shown in Fig. 4(a). The 3 o'clock position is assigned as the starting point of δ and δ increases counterclockwise. The radius of the circle is r, which is inversely proportional to the total reactance X_T. The vector fields on the circle under different scenarios are given in Fig. 4, which are as follows.

1) If $r < \omega_r$, no fixed point exists and the flow will loop counterclockwise forever, i.e., the system keeps oscillating, as shown in Fig. 4(a).
2) If $r > \omega_r$, there are two fixed points, which can be obtained by letting $f(\delta) = 0$

$$\delta_1^* = \arcsin\left(\frac{\omega_r}{r}\right), \quad \delta_2^* = \pi - \arcsin\left(\frac{\omega_r}{r}\right). \tag{20}$$

Since $r > \omega_r > 0$, the two fixed points are on the upper half of the circle, as shown in Fig. 4(b). The linear stability of any fixed point δ^* is determined by

$$f'(\delta^*) = -r \cos(\delta^*). \tag{21}$$

For first-order nonlinear systems, the fixed point is stable if $f'(\delta^*) < 0$ and unstable if $f'(\delta^*) > 0$ [41]. Evidently, δ_1^* and δ_2^* are the stable and unstable fixed points, respectively, which are marked as a solid dot and an open circle in Fig. 4(b), respectively. Henceforth, the two fixed points are referred to as $\delta_{\text{sf}} := \delta_1^*$ and $\delta_{\text{uf}} := \delta_2^*$. Different from the scenario without fixed points, the existence of fixed points fundamentally changes the dynamics of the system. As can be seen from Fig. 4(b), the flow is attracted by the stable fixed point and repelled by the unstable fixed point. As long as there is a stable fixed point, the system will finally be stabilized at that point.
3) If $r = \omega_r$, there is one fixed point at $\delta = \pi/2$, as shown in Fig. 4(c). This point is half-stable, since it is attracting from the right and repelling from the left. This phenomenon is also called saddle-node bifurcation [41]. In the application of transient stability assessment of dVOC, the half-stable case can be treated as a special stable case and will not be discussed separately. This is because the half-stable case predicted by the model (which is usually built on some simplifications, e.g., neglect of parasitic resistances) is usually stable in the real system considering the damping provided by the parasitic resistances in transformer and transmission lines.

Fig. 4(d) shows a family of vector fields including all three cases in Fig. 4(a) (c) with ω_r fixed and different values of r. Based on (20), the relative value of ω_r and r can be visualized as the distance (angular difference) between the two fixed points. As r decreases, the two fixed points approach each other, collide, and finally mutually annihilate, and then the system begin to oscillate.

For comparison, the two fault cases discussed in Section II are analyzed for dVOC using vector fields on the circle. The parameters of the dVOC used in the study are provided in Table I as dVOC #1. Similar to droop control, the analysis is limited to faults that do not trigger the overcurrent limit of the converter. The current limiting control scheme for dVOC is still an open question and out of scope of this article. However, the common practice for droop-based grid-forming control, which is to transition the control structure to a PLL-synchronized current control when the overcurrent limit is triggered [31], [35], is equally applicable for dVOC-based inverter. Under this extreme condition, the transient stability characteristics will be largely determined by the PLL design [36], [37].

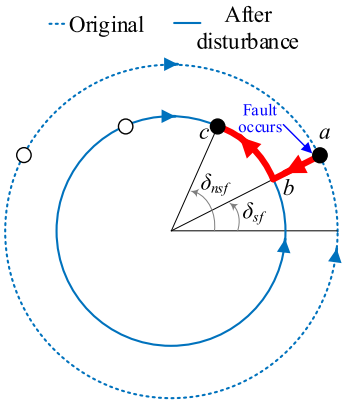

Fig. 5. Vector fields of dVOC under out-of-service fault.

B. Case 1: Equilibrium Point Exists During Fault

When the second transmission line is out of service, the total reactance increases to X_{Tos}. Since r is inversely proportional to the total reactance, a smaller circle is created after disturbance. This new r is denoted as r_{os}. Since equilibrium point exists ($P^* < P_{\max}$), ω_r and r_{os} have the following relationship:

$$\frac{\omega_r}{r_{os}} = \frac{P^*}{\frac{3VV_g}{X_{Tos}}} = \frac{P^*}{P_{\max}} < 1. \tag{22}$$

Based on previous analysis, if $\omega_r < r_{os}$, the system has two fixed points. Fig. 5 shows the vector fields before and after the disturbance. There are two new fixed points δ_{nsf} and δ_{nuf}

$$\delta_{\text{nsf}} = \arcsin\left(\frac{\omega_r}{r_{os}}\right), \quad \delta_{\text{nuf}} = \pi - \arcsin\left(\frac{\omega_r}{r_{os}}\right). \tag{23}$$

Originally, the system operates at a stable fixed point a with a power angle of δ_{sf}. After out-of-service fault, the operating point moves to point b on the new vector field. Then, the operating point flows to the new stable point c with a power angle of δ_{nsf}.

C. Case 2: No Equilibrium Point During Fault

When three-phase to ground short-circuit fault occurs, the total reactance increases substantially to X_{Tsc}. Consequently, r decreases and this new r is denoted as r_{sc}. Since $P^* > P_{\max}$, (i.e., $\omega_r > r_{\text{sc}}$) during the fault, no fixed point exists, meaning the system will oscillate and synchronism is lost. Referring to Fig. 6. the system operates at point a and moves to point b after fault. When the fault is cleared, based on different fault-clearing angles, there are two possible scenarios. In Fig. 6(a), the fault is cleared at point c with a power angle smaller than δ_{nuf}. In this case, the operating point moves to point d on the new vector field and flows to the new stable fixed point e clockwise. In Fig. 6(b), the fault is cleared after δ_{nuf}, and the operating point moves to point d on the new vector field, and then it flows to the new stable fixed point e counterclockwise. It can be seen that regardless of when the fault is cleared, the system is always stable. The only difference is that if fault is cleared before δ_{nuf}, the system will be stable without major oscillation; otherwise, the system

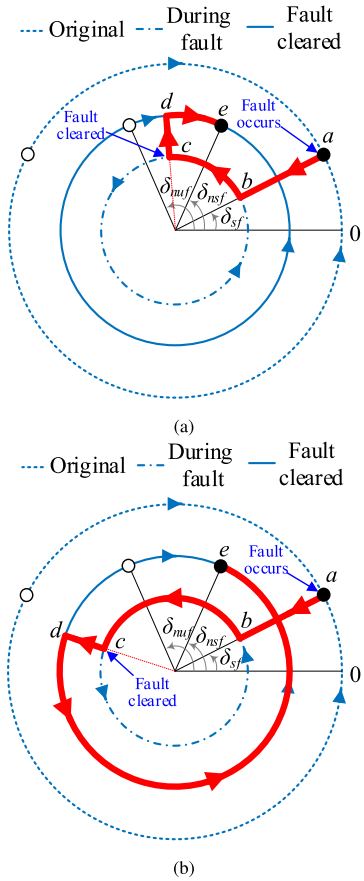

Fig. 6. Vector fields of dVOC under short-circuit fault. (a) Fault cleared before δ_{nuf}. (b) Fault cleared after δ_{nuf}.

undergoes about one cycle of oscillation before reaching the new stable operating point.

Another potential case, which is not shown in Fig. 6, is that the system may oscillate for k ($k = 1, 2, 3\ldots$) cycles during fault, but once the fault is cleared, the system readily retains stable operation by moving to the new operating point.

Based on (23), the expression for the critical fault-clearing angle δ_{nuf} can be rewritten as

$$\delta_{\text{nuf}} = \pi - \arcsin\left(\frac{\omega_r}{r_{os}}\right) = \pi - \arcsin\left(\frac{X_{Tos}P^*}{3VV_g}\right) \tag{24}$$

which is independent of the dVOC control parameters or fault conditions and is solely dependent on postfault system parameters. Compared to droop control, this greatly simplifies the protection system design, and the corresponding critical fault-clearing time can be obtained as

$$T_c = \int_{\delta_{\text{sf}}}^{\delta_{\text{nuf}}} \frac{dt}{d\delta} d\delta = \int_{\delta_{\text{sf}}}^{\delta_{\text{nuf}}} \frac{d\delta}{\omega_r - r_{\text{sc}} \sin\delta} = F_t(\delta_{\text{nuf}}) - F_t(\delta_{\text{sf}}) \tag{25}$$

where $F_t(\delta)$ is the antiderivative for $1/(\omega_r - r_{\text{sc}} \sin\delta)$ and it is given as [41]

$$F_t(\delta) = \frac{2}{\sqrt{\omega_r^2 - r_{\text{sc}}^2}} \arctan\left(\frac{\omega_r \tan(\delta/2) - r_{\text{sc}}}{\sqrt{\omega_r^2 - r_{\text{sc}}^2}}\right). \tag{26}$$

Similarly, the oscillation cycle during fault can be analytically derived as

$$T_{rf} = \int_0^{2\pi} \frac{d\delta}{\omega_r - r_{\rm sc}\sin\delta} = \frac{2\pi}{\sqrt{\omega_r^2 - r_{\rm sc}^2}}. \tag{27}$$

Again, the critical time is only the boundary for whether the system moves clockwise [see Fig. 6(a)] or counter clockwise [see Fig. 6(b)] to reach the new stable fixed point.

Compared to droop control, there are a number of fundamental differences in the transient stability of dVOC, which are as follows.

1) As long as $P^* < P_{\rm max}$ after disturbance, the dVOC-based grid-connected inverter system will be stable.
2) After disturbance, the power angle evolves monotonically toward the new fixed point without any overshoots and oscillations.
3) For dVOC, the critical fault-clearing angle is not related with control parameters. If fault is cleared before the critical angle, the system will be stabilized without major oscillation; if it is cleared after the critical angle, the system can still be stabilized within one oscillation cycle. The system can always resynchronize with the grid once the fault is cleared, even if it has been oscillating for an arbitrary number of cycles.

V. Coupling Effect of Active and Reactive Power on Transient Stability of dVOC

Although dVOC cannot achieve perfectly constant voltage regulation, the limit-cycle dynamics of dVOC can tightly regulate the voltage around a nominal value. The analysis in Section IV assumes that dVOC is appropriately designed for weak grid operation and its voltage amplitude V is approximated as a constant value (i.e., that VOC #1 design parameters from Table I are used). This assumption substantially simplifies the transient stability assessment without sacrificing noticeable accuracy. However, a highly precise model that can be used to quantitatively analyze the impact of the voltage amplitude dynamics is valuable, especially for applications with high accuracy requirements that are insensitive to computational burden.

In [38]–[40], the impact of reactive power control on transient stability of droop control is analyzed by using $\dot\delta - \delta$ and $\delta - V$ curves. In droop control, the active and reactive power control loops are separately and explicitly implemented, whereas dVOC utilizes the time-domain Hopf oscillator dynamics to control the inverter and does not have explicit active and reactive power control loops. Nonetheless, we will demonstrate that a large-signal model that includes both the power angle δ and voltage amplitude V dynamics can be derived in the polar coordinates, which captures the cross-coupling of active and reactive power in dVOC. Based on this large-signal model, the $\dot\delta - \delta$ and $\delta - V$ curves can be utilized to study the coupling effect of active and reactive power on transient stability of dVOC.

As noted in Section III, a $P_o - \omega$ and $Q_o - V$ droop-like oscillator based control is chosen in this article. A large-signal model that links the active power P_o and power angle δ has been established in (16). It can be further observed that P_o is not only a function of δ, but also coupled with voltage amplitude V. Similarly, the reactive power Q_o is also a function of both δ and V. The reactive power flow from the inverter to the infinite bus Q_o can be derived as

$$Q_o = \frac{3(V^2 - VV_g\cos\delta)}{X_T}. \tag{28}$$

Substituting (28) into the dVOC voltage amplitude dynamic equation (13), we have

$$\dot V = \frac{\xi}{\kappa_v^2} V\left(2\,V_{\rm nom}^2 - 2\,V^2\right) - \frac{\kappa_v\kappa_i}{3CV}\left(\frac{3(V^2 - VV_g\cos\delta)}{X_T} - Q^*\right) \tag{29}$$

which shows that the reactive power of dVOC is not only related with the static value of V and δ, but also the first derivative of V. Repeating (16) for convenience

$$\dot\delta = \frac{\kappa_v\kappa_i}{3CV^2}\left(P^* - \frac{3VV_g}{X_T}\sin\delta\right). \tag{30}$$

The complete large-signal model of a dVOC-based grid-connected inverter system is given by (29) and (30), which clearly shows the cross-coupling between active and reactive power through the V and δ dynamics. Since the expressions for both δ or V are nonlinear differential equations, an analytical solution does not exist. With both the dynamics of V and δ considered, the complete large-signal model now has a two-dimensional phase space and the vector field on the circle method is no longer applicable. To assess the transient stability of dVOC using this model, the two coupled nonlinear differential equations need to be numerically solved, and the $\dot\delta - \delta$ and $V - \delta$ curve can be plotted.

The steady-state voltage of dVOC can be obtained by solving $\dot V = 0$ in (13), and then the maximum voltage deviation from its nominal value can be derived. Defining $V_u = V/V_{\rm nom}$ and assuming $Q^* = 0$ (the value of Q^* will not change the droop slope [23]), the maximum voltage droop $\Delta V_{\rm umax}$ (p.u.) can be calculated when Q_o is the rated value (1 p.u.)

$$\Delta V_{\rm umax} = 1 - \sqrt{\frac{1 + \sqrt{1 - \frac{\sqrt{2}}{C\xi}}}{2}}. \tag{31}$$

Therefore, the voltage droop can be designed via the dVOC parameters C and ξ using (31). As a comparison, two sets of dVOC parameters are provided in Table I. With dVOC #1, the voltage is tightly regulated ($\Delta V_{\rm umax} = 2.07\%$), whereas dVOC #2, $\Delta V_{\rm umax} = 8.07\%$, is an exaggerated design that highlights the impact of voltage dynamics on transient stability.

Next, the transmission line out-of-service fault scenario presented earlier is revisited here in the context of transient stability analysis of dVOC using $\dot\delta - \delta$ and $V - \delta$ curves (Figs. 7 and 8, respectively). To emphasize the cross-coupling effect, the results considering V as a constant value are also provided. In Fig. 7, the blue solid line denotes the transient response of the inverter with dVOC #1 under the constant voltage assumption. The system is initially at a stable fixed point $\delta_{\rm sf}$ and later flows to the new stable fixed point $\delta_{\rm nsf}$, which corresponds to the analysis

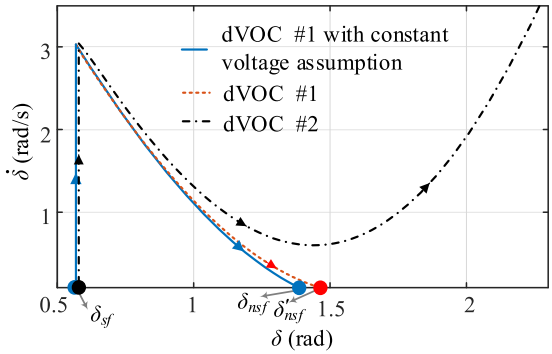

Fig. 7. Phase portrait of dVOC under transmission line out-of-service fault considering the voltage dynamics.

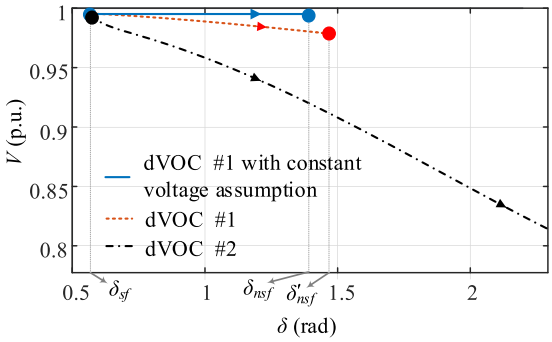

Fig. 8. $V-\delta$ curve of dVOC under transmission line out-of-service fault.

in Section IV. The red dotted line denotes the phase portrait when the coupling effect between active and reactive power is included. It follows a very close trajectory as the blue solid line, and the system is finally stabilized at a slightly higher angle δ'_{nsf}. This can be explained by the red dotted $V-\delta$ curve in Fig. 8. It can be seen that when the coupling effect is considered, a slight voltage drop relative to its initial value can be observed when the system is finally stabilized at δ'_{nsf}. This voltage drop is imposed by reactive power regulation of dVOC when the transient disturbance occurs. According to (3), the decrease of V results in the decrease of $P_{\max}$, which makes the new stable fixed point higher. Under extreme conditions, the voltage drop imposed by the reactive power regulation can be significant and lead to substantial decrease of $P_{\max}$ and even $P_{\max} < P^*$, which leads to the loss of synchronism, as shown in the dVOC #2 case in Figs. 7 and 8. The plots show that with different dVOC parameters, the initial power angle and voltage amplitude before the transient disturbance are slightly different, even with the same power system parameters (i.e., X_T and X_{Tos}). This is because different dVOC designs exhibit different voltage droop characteristics that lead to different steady-state voltages, which causes different steady-state power angles.

The analysis above reveals the adverse impact of the cross-coupling between active and reactive power in a dVOC-based grid-connected inverter. When grid disturbances occur, the underlying reactive power regulation in dVOC will introduce a voltage drop and deteriorate the transient stability. Hence, for

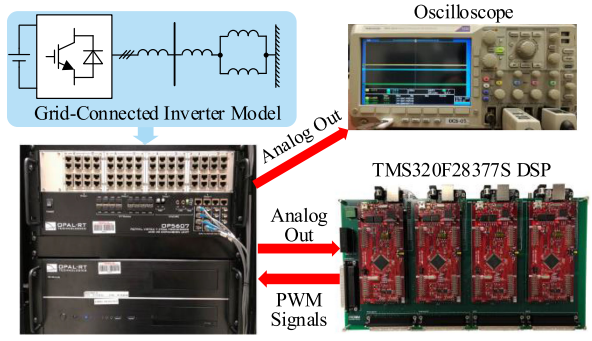

Fig. 9. OPAL-RT-based real-time C-HIL testbed.

the sake of improved transient stability, the dVOC parameters should be designed to have a tight voltage regulation (such as dVOC #1) under weak grid conditions. This design is also beneficial in terms of voltage support for the weak grid power system, which is similar to the rationale of operating droop controlled inverters in AVC mode.

The closeness of the two phase portraits (dVOC #1 and dVOC #1 with constant voltage assumption) validates that with a tightly regulated dVOC, the system will dominantly show a first-order response and the V dynamics and reactive power coupling effect can be ignored without sacrificing accuracy significantly. By neglecting the voltage amplitude dynamics, the transient stability assessment can be simplified considerably by using the vector field on the circle method since no nonlinear equations need to be solved (see Section IV). This assessment provides very straightforward design guidelines for protection system design. However, since vector field on the circle method does not consider the adverse impact of the cross-coupling of active and reactive power, an adequate safety margin should be considered when designing system protection using this approach. Last but not least, the complete large-signal model given by (29) and (30) is universal and can be applicable to any dVOC-based grid-connected inverter system, although the computational cost is high.

VI. Experimental Validation

OPAL-RT-based HIL simulation is a powerful tool for control algorithms verification and analysis in power electronics systems [43]–[45]. Compared to hardware test, HIL simulations provide a more flexible and comprehensive solution, especially for research on faults in power electronics systems considering the safety issues, cost, and complexity of introducing faults in the lab environment.

To validate the transient stability analysis, a test system is built on an OPAL-RT-based real-time C-HIL setup using industry-grade control hardware, as shown in Fig. 9, with simulation parameters given in Table I. In Table I, L_l, L_{tr}, L_{g1}, L_{g2}, and L_Δ are the corresponding inductances of X_l, X_{tr}, X_{g1}, X_{g2}, and X_Δ, respectively. For droop control implementation, the LPF cutoff frequency ω_c is designed for inertia emulation rather than simply for noise and power fluctuations suppression [39], [40], whereas the inner voltage control and LC filter parameters

TABLE I
TRANSIENT STABILITY TEST SYSTEM PARAMETERS

Parameter		Value
System	P^*, Q^*, V_g, ω_o	150kW, 0, 277V(RMS), 120πrad/s
	L_l	305μF
Droop	m_p, ω_c	1/12500, 1.5rad/s
dVOC #1	L, C, ξ	46.908μH, 0.15F, 60 1/sV^2
	X_{nom}, κ_v, κ_i	1, 277, 0.00554
dVOC #2	L, C, ξ	46.908μH, 0.15F, 18 1/sV^2
	X_{nom}, κ_v, κ_i	1, 277, 0.00554
Case #1	L_{tr}, L_{g1}, L_{g2}	81μH, 3.56mH, 3.56mH
Case #2	$L_{tr}, L_{g1}, L_{g2}, L_\Delta$	2.5mH, 850μH, 2.5mH, 2.0mH

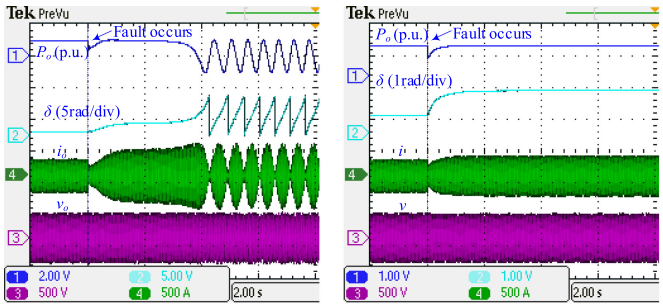

(a) (b)

Fig. 10. Inverter response with an out-of-service fault. (a) Droop control. (b) dVOC.

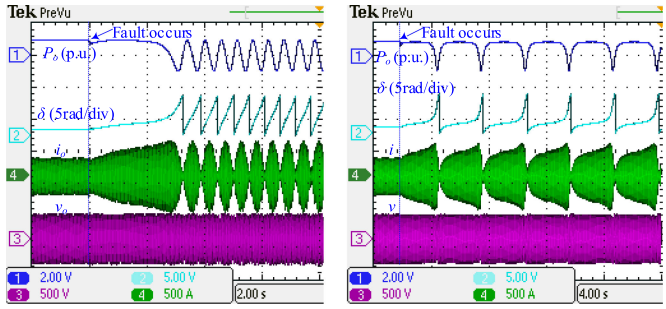

(a) (b)

Fig. 11. Inverter response with a three-phase short-circuit fault. (a) Droop control. (b) dVOC.

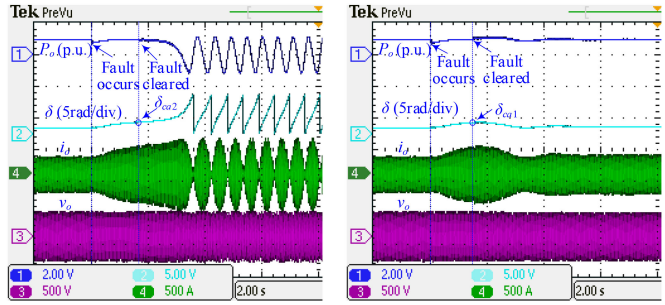

(a) (b)

Fig. 12. Inverter response with droop control under different fault-clearing schemes. (a) Fault cleared after CCA. (b) Fault cleared before CCA.

for droop control are omitted for brevity. Field-programmable gate array (FPGA) based simulator with a simulation time step of 500 ns is used to simulate the grid-connected inverter system. An industry-grade digital signal processor (DSP) TMS320F28377S from Texas Instruments is used for implementation of the inverter control algorithm. Simulated states, such as voltages and currents, are sent to the DSP via analog output modules on OPAL-RT simulator, and the PWM signals are generated and sent to the simulator. The switching and sampling frequency are 10 and 20 kHz, respectively.

Fig. 10 shows the test results for Case 1 for both droop control and dVOC #1. Based on the parameters in Table I, when the second transmission line is out of service, the total reactance increases and $P_{\max}$ is reduced to 153.8 kW; still $P^* < P_{\max}$ is satisfied, i.e., equilibrium point exists. As shown in Fig. 10(a), the active power P_o, power angle δ, and output current i_o begin to oscillate severely after the fault is introduced, which suggests that the inverter loses synchronism during the fault with droop control. In Fig. 10(b), the inverter with dVOC can rapidly settle down to a new steady state in an overdamped fashion, which is consistent with a first-order system response. The results validate the conclusion that transient stability issues may arise for droop control even if equilibrium point exists after disturbance, whereas for dVOC, synchronism is maintained as long as equilibrium point exists.

Next, Case 2 is considered. Under the three-phase short-circuit fault, the equivalent total reactance increases significantly. The corresponding $P_{\max} = 141.0$ kW is considerably lower than P^*. As shown in Fig. 11, severe oscillations occur with both droop control and dVOC #1, i.e., both of them lose synchronism, as expected. For dVOC, the oscillation cycle during fault is calculated as 2.78 s using (27). In Fig. 11(b), the oscillation cycle is around 2.90 s, which is very close to the theoretical prediction. To prevent system collapse, protective relay should open circuit breakers and isolate the second transmission line. For droop control, the CCA is found to be $\delta_{\text{cca}} = 1.78$ rad using numerical methods. Fig. 12(a) shows the result for droop control with a slow fault-clearing scheme (fault-clearing angle $\delta_{ca2} = 2$ rad), in which the fault is cleared after δ_{cca} and the inverter loses synchronism. In Fig. 12(b), with a faster fault-clearing scheme (fault-clearing angle $\delta_{ca1} = 1.6$ rad), loss of synchronism is avoided. In Fig. 12(b), small oscillations can be observed in P_o, δ, and i_o before the inverter finally reaches a new steady state, which validates the conclusion in Section II. For dVOC, the critical fault-clearing time T_c is calculated as 1.73 s using (25). Fig. 13 shows the results for dVOC with the fault cleared within the first cycle of oscillation. In Fig. 13(a), the fault is cleared with a fault-clearing time of 2 s, the inverter resynchronizes with the grid after one cycle of oscillation. In Fig. 13(b), the fault is cleared at 1.5 s and synchronism can be maintained without major oscillations. Fig. 14 shows the result when fault is cleared after two cycles of oscillation. The inverter can still resynchronize the grid. Experimental results agree well with the theoretical analysis and show that with dVOC control, there is no considerable voltage change in the inverter terminal voltage with different transient disturbances.

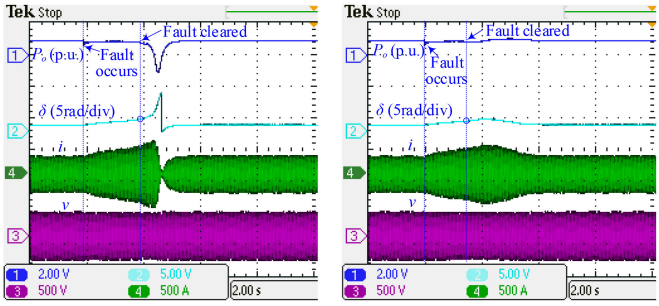

Fig. 13. Inverter response with dVOC under fault-clearing schemes within the first cycle of oscillation. (a) Fault cleared after δ_{nuf}. (b) Fault cleared before δ_{nuf}.

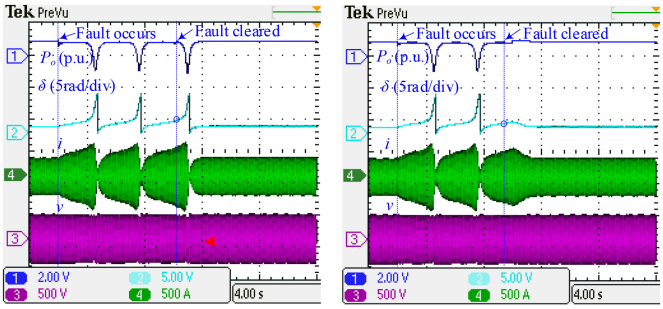

Fig. 14. Inverter response with dVOC under fault-clearing schemes after two cycles of oscillation. (a) Fault cleared after $4\pi + \delta_{\text{nuf}}$. (b) Fault cleared before $4\pi + \delta_{\text{nuf}}$.

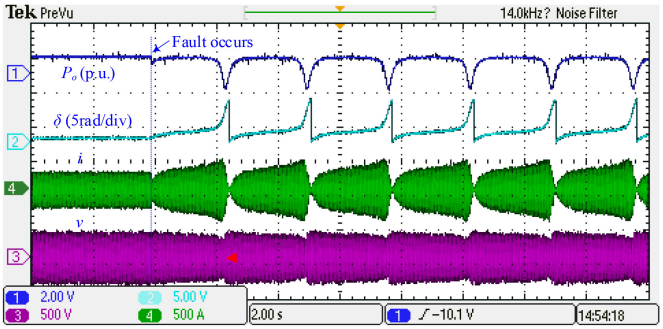

Fig. 15. Voltage amplitude dynamics impact validation with dVOC #2.

The adverse effect of the voltage dynamics on transient stability of dVOC is validated in Fig. 15. With dVOC #2, which has an exaggeratedly wide range of voltage regulation, synchronism is lost when the same transmission line considered in Fig. 10(b) loses service. The result validates that a tightly regulated dVOC exhibits better transient stability.

VII. Conclusion

A comparative transient stability analysis of droop control and an emerging nonlinear grid-forming controller, dVOC, is carried out in this article. The power angle dynamic model of dVOC is derived and is shown to be a first-order nonuniform oscillator. Salient transient stability features of dVOC under different fault conditions and fault-clearing schemes are analyzed by using a novel graphical method, i.e., vector field on the circle. This article shows that dVOC is superior to droop control in terms of transient stability when subjected to large grid disturbances. Finally, this work shows that a tightly regulated dVOC improves the transient stability of dVOC, providing a new perspective in appropriate dVOC parameters design.

References

[1] J. M. Guerrero, J. C. Vasquez, J. Matas, L. G. de Vicuna, and M. Castilla, "Hierarchical control of droop-controlled ac and dc microgrids—A general approach toward standardization," *IEEE Trans. Ind. Electron.*, vol. 58, no. 1, pp. 158–172, Jan. 2011.

[2] J. Rocabert, A. Luna, F. Blaabjerg, and P. Rodriguez, "Control of power converters in ac microgrids," *IEEE Trans. Power Electron.*, vol. 27, no. 11, pp. 4734–4749, Nov. 2012.

[3] H. Beck and R. Hesse, "Virtual synchronous machine," in *Proc. 9th Int. Conf. Elect. Power Qual. Utilisation*, Oct. 2007, pp. 1–6.

[4] H. Wu *et al.*, "Small-signal modeling and parameters design for virtual synchronous generators," *IEEE Trans. Ind. Electron.*, vol. 63, no. 7, pp. 4292–4303, Jul. 2016.

[5] B. Johnson, M. Rodriguez, M. Sinha, and S. Dhople, "Comparison of virtual oscillator and droop control," in *Proc. IEEE 18th Workshop Control Model. Power Electron.*, 2017, pp. 1–6.

[6] H. Yu, M. A. Awal, H. Tu, Y. Du, S. Lukic, and I. Husain, "Passivity-oriented discrete-time voltage controller design for grid-forming inverters," in *Proc. IEEE Energy Convers. Congr. Expo.*, 2019, pp. 469–475.

[7] S. D'Arco and J. A. Suul, "Equivalence of virtual synchronous machines and frequency-droops for converter-based microgrids," *IEEE Trans. Smart Grid*, vol. 5, no. 1, pp. 394–395, Jan. 2014.

[8] N. Pogaku, M. Prodanovic, and T. C. Green, "Modeling, analysis and testing of autonomous operation of an inverter-based microgrid," *IEEE Trans. Power Electron.*, vol. 22, no. 2, pp. 613–625, Mar. 2007.

[9] S. V. Dhople, B. B. Johnson, and A. O. Hamadeh, "Virtual oscillator control for voltage source inverters," in *Proc. 51st Annu. Allerton Conf. Commun., Control, Comput.*, 2013, pp. 1359–1363.

[10] S. V. Dhople, B. B. Johnson, F. Dorfler, and A. O. Hamadeh, "Synchronization of nonlinear circuits in dynamic electrical networks with general topologies," *IEEE Trans. Circuits Syst. I, Reg. Papers*, vol. 61, no. 9, pp. 2677–2690, Sep. 2014.

[11] B. B. Johnson, S. V. Dhople, A. O. Hamadeh, and P. T. Krein, "Synchronization of parallel single-phase inverters with virtual oscillator control," *IEEE Trans. Power Electron.*, vol. 29, no. 11, pp. 6124–6138, Nov. 2014.

[12] B. B. Johnson, M. Sinha, N. G. Ainsworth, F. Dorfler, and S. V. Dhople, "Synthesizing virtual oscillators to control islanded inverters," *IEEE Trans. Power Electron.*, vol. 31, no. 8, pp. 6002–6015, Aug. 2016.

[13] M. Sinha, F. Dorfler, B. B. Johnson, and S. V. Dhople, "Uncovering droop control laws embedded within the nonlinear dynamics of Van der Pol oscillators," *IEEE Trans. Control Netw. Syst.*, vol. 4, no. 2, pp. 347–358, Jun. 2017.

[14] M. Lu, G.-S. Seo, M. Sinha, F. Rodriguez, S. Dhople, and B. Johnson, "Adaptation of commercial current-controlled inverters for operation with virtual oscillator control," in *Proc. IEEE Appl. Power Electron. Conf. Expo.*, 2019, pp. 3427–3432.

[15] D. Raisz, T. T. Thai, and A. Monti, "Power control of virtual oscillator controlled inverters in grid-connected mode," *IEEE Trans. Power Electron.*, vol. 34, no. 6, pp. 5916–5926, Jun. 2019.

[16] M. A. Awal, H. Yu, H. Tu, S. M. Lukic, and I. Husain, "Hierarchical control for virtual oscillator based grid-connected and islanded microgrids," *IEEE Trans. Power Electron.*, vol. 35, no. 1, pp. 988–1001, Jan. 2020.

[17] Z. Shi, J. Li, H. I. Nurdin, and J. E. Fletcher, "Comparison of virtual oscillator and droop controlled islanded three-phase microgrids," *IEEE Trans. Energy Convers.*, vol. 34, no. 4, pp. 1769–1780, Dec. 2019.

[18] H. Yu, M. A. Awal, H. Tu, Y. Du, S. Lukic, and I. Husain, "A virtual impedance scheme for voltage harmonics suppression in virtual oscillator controlled islanded microgrids," in *Proc. IEEE Appl. Power Electron. Conf. Expo.*, 2020, pp. 609–615.

[19] J. W. Simpson-Porco, F. Dörfler, and F. Bullo, "Synchronization and power sharing for droop-controlled inverters in islanded microgrids," *Automatica*, vol. 49, no. 9, pp. 2603–2611, 2013.

[20] M. Colombino, D. Gro, J. Brouillon, and F. Drfler, "Global phase and magnitude synchronization of coupled oscillators with application to the control of grid-forming power inverters," *IEEE Trans. Autom. Control*, vol. 64, no. 11, pp. 4496–4511, Nov. 2019.
[21] D. Gro, M. Colombino, J. Brouillon, and F. Drfler, "The effect of transmission-line dynamics on grid-forming dispatchable virtual oscillator control," *IEEE Trans. Control Netw. Syst.*, vol. 6, no. 3, pp. 1148–1160, Sep. 2019.
[22] G. Seo, M. Colombino, I. Subotic, B. Johnson, D. Gro, and F. Drfler, "Dispatchable virtual oscillator control for decentralized inverter-dominated power systems: Analysis and experiments," in *Proc. IEEE Appl. Power Electron. Conf. Expo.*, 2019, pp. 561–566.
[23] M. Lu, S. Dutta, V. Purba, S. Dhople, and B. Johnson, "A grid-compatible virtual oscillator controller: Analysis and design," in *Proc. IEEE Energy Convers. Congr. Expo.*, Sep. 2019, pp. 2643–2649.
[24] M. A. Awal, H. Yu, I. Husain, W. Yu, and S. M. Lukic, "Selective harmonic current rejection for virtual oscillator controlled grid-forming voltage source converters," *IEEE Trans. Power Electron.*, vol. 35, no. 8, pp. 8805–8818, Aug. 2020.
[25] P. Kundur, N. J. Balu, and M. G. Lauby, *Power System Stability and Control*, vol. 7. New York, NY, USA: McGraw-Hill, 1994.
[26] J. Alipoor, Y. Miura, and T. Ise, "Power system stabilization using virtual synchronous generator with alternating moment of inertia," *IEEE J. Emerg. Sel. Topics Power Electron.*, vol. 3, no. 2, pp. 451–458, Jun. 2015.
[27] L. Xiong *et al.*, "Static synchronous generator model: A new perspective to investigate dynamic characteristics and stability issues of grid-tied PWM inverter," *IEEE Trans. Power Electron.*, vol. 31, no. 9, pp. 6264–6280, Sep. 2016.
[28] Z. Shuai, C. Shen, X. Liu, Z. Li, and Z. J. Shen, "Transient angle stability of virtual synchronous generators using Lyapunovs direct method," *IEEE Trans. Smart Grid*, vol. 10, no. 4, pp. 4648–4661, Jul. 2019.
[29] H. Wu and X. Wang, "A mode-adaptive power-angle control method for transient stability enhancement of virtual synchronous generators," *IEEE J. Emerg. Sel. Topics Power Electron.*, vol. 8, no. 2, pp. 1034–1049, Jun. 2020.
[30] H. Wu and X. Wang, "Transient angle stability analysis of grid-connected converters with the first-order active power loop," in *Proc. IEEE Appl. Power Electron. Conf. Expo.*, 2018, pp. 3011–3016.
[31] H. Wu and X. Wang, "Design-oriented transient stability analysis of grid-connected converters with power synchronization control," *IEEE Trans. Ind. Electron.*, vol. 66, no. 8, pp. 6473–6482, Aug. 2019.
[32] A. D. Paquette and D. M. Divan, "Virtual impedance current limiting for inverters in microgrids with synchronous generators," *IEEE Trans. Ind. Appl.*, vol. 51, no. 2, pp. 1630–1638, Mar./Apr. 2015.
[33] L. Huang, H. Xin, Z. Wang, L. Zhang, K. Wu, and J. Hu, "Transient stability analysis and control design of droop-controlled voltage source converters considering current limitation," *IEEE Trans. Smart Grid*, vol. 10, no. 1, pp. 578–591, Jan. 2019.
[34] H. Xin, L. Huang, L. Zhang, Z. Wang, and J. Hu, "Synchronous instability mechanism of PF droop-controlled voltage source converter caused by current saturation," *IEEE Trans. Power Syst.*, vol. 31, no. 6, pp. 5206–5207, Nov. 2016.
[35] L. Zhang, L. Harnefors, and H. Nee, "Power-synchronization control of grid-connected voltage-source converters," *IEEE Trans. Power Syst.*, vol. 25, no. 2, pp. 809–820, May 2010.
[36] H. Wu and X. Wang, "Design-oriented transient stability analysis of PLL-synchronized voltage-source converters," *IEEE Trans. Power Electron.*, vol. 35, no. 4, pp. 3573–3589, Apr. 2020.
[37] M. G. Taul, X. Wang, P. Davari, and F. Blaabjerg, "An overview of assessment methods for synchronization stability of grid-connected converters under severe symmetrical grid faults," *IEEE Trans. Power Electron.*, vol. 34, no. 10, pp. 9655–9670, Oct. 2019.
[38] D. Pan, X. Wang, F. Liu, and R. Shi, "Transient stability impact of reactive power control on grid-connected converters," in *Proc. IEEE Energy Convers. Congr. Expo.*, 2019, pp. 4311–4316.
[39] D. Pan, X. Wang, F. Liu, and R. Shi, "Transient stability analysis of droop-controlled grid-connected converters with inertia emulating low-pass filters," in *Proc. IEEE Energy Convers. Congr. Expo.*, 2019, pp. 34–40.
[40] D. Pan, X. Wang, F. Liu, and R. Shi, "Transient stability of voltage-source converters with grid-forming control: A design-oriented study," *IEEE J. Emerg. Sel. Topics Power Electron.*, vol. 8, no. 2, pp. 1019–1033, Jun. 2020.
[41] S. H. Strogatz, *Nonlinear Dynamics and Chaos: With Applications to Physics, Biology, Chemistry, and Engineering*. Boulder, CO, USA: Westview, 2015.
[42] M. Sinha, S. Dhople, B. Johnson, N. Ainsworth, and F. Dörfler, "Nonlinear supersets to droop control," in *Proc. IEEE 16th Workshop Control Model. Power Electron.*, 2015, pp. 1–6.
[43] Q. Ye, R. Mo, and H. Li, "Low-frequency resonance suppression of a dual-active-bridge dc/dc converter enabled dc microgrid," *IEEE J. Emerg. Sel. Topics Power Electron.*, vol. 5, no. 3, pp. 982–994, Sep. 2017.
[44] H. Tu, Y. Du, H. Yu, A. Dubey, S. Lukic, and G. Karsai, "Resilient information architecture platform for the smart grid (RIAPS): A novel open-source platform for microgrid control," *IEEE Trans. Ind. Electron.*, early access, doi: 10.1109/TIE.2019.2952803.
[45] Y. Du, H. Tu, H. Yu, and S. Lukic, "Accurate consensus-based distributed averaging with variable time delay in support of distributed secondary control algorithms," *IEEE Trans. Smart Grid*, vol. 11, no. 4, pp. 2918–2928, Jul. 2020.

Hui Yu (Student Member, IEEE) received the bachelor's and master's degrees in electrical engineering from the Huazhong University of Science and Technology, Wuhan, China, in 2013 and 2016, respectively. He is currently working toward the Ph.D. degree with the Future Renewable Electric Energy Delivery and Management Systems Center, North Carolina State University, Raleigh, NC, USA.

His research interests include power electronics converter modeling, design and control in microgrids, and energy storage systems.

Mr. Yu was a recipient of the Outstanding Presentation Award of the 2018 IEEE Applied Power Electronics Conference.

M. A. Awal (Student Member, IEEE) received the B.S. degree in electrical and electronic engineering from the Bangladesh University of Engineering and Technology, Dhaka, Bangladesh, in 2014. He is currently working toward the Ph.D. degree with the Future Renewable Electric Energy Delivery and Management Systems Center, North Carolina State University, Raleigh, NC, USA.

His research interests include converter-level and system-level control strategies for microgrids and networked power electronics systems.

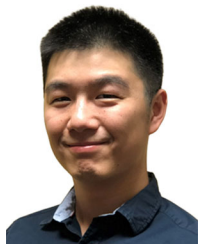

Hao Tu (Student Member, IEEE) received the bachelor's degree from Xi'an Jiaotong University, Xi'an, China, in 2012, the master's degree from RWTH Aachen University, Aachen, Germany, in 2015, and the Ph.D. degree from North Carolina State University, Raleigh, NC, USA, in 2020, all in electrical engineering.

He is currently a Research Assistant Professor with the National Science Foundation Future Renewable Electric Energy Delivery and Management Systems Engineering Research Center, North Carolina State University. His research interests include control of power electronics converters, energy storage systems, and microgrids.

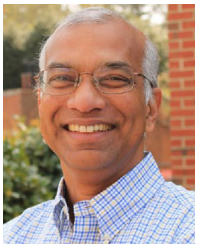

Iqbal Husain (Fellow, IEEE) received the Ph.D. degree in electrical engineering from Texas A&M University, College Station, TX, USA, in 1993.

He is currently the Director of the Future Renewable Electric Energy Delivery and Management National Science Foundation Engineering Center and the ABB Distinguished Professor with the Department of Electrical and Computer Engineering, North Carolina (NC) State University, Raleigh, NC. Prior to joining NC State University, he was with the University of Akron where he built a successful power electronics and motor drives program. He was a Visiting Professor with Oregon State University, Corvallis, OR, USA, in 2001. He has developed innovative graduate and undergraduate courses on electric and hybrid vehicles and authored or coauthored the book *Electric and Hybrid Vehicles: Design Fundamentals* (CRC Press, 2010) on this topic. He expertises in the areas of power electronics, electric machines, motor drives, and system controls. His research is also focused on power electronics and drives integration into power and transportation systems.

Dr. Husain was the recipient of the 2006 SAE Vincent Bendix Automotive Electronics Engineering Award, the 2004 College of Engineering Outstanding Researcher Award, the 2000 IEEE Third Millennium Medal, and the 1998 IEEE-IAS Outstanding Young Member Award. He is the Past Editor-in-Chief for the *IEEE Electrification Magazine*.

Srdjan Lukic (Senior Member, IEEE) received the Ph.D. degree in electrical engineering from the Illinois Institute of Technology, Chicago, IL, USA, in 2008.

He is currently a Professor with the Department of Electrical and Computer Engineering, North Carolina State University, Raleigh, NC, USA. He serves as the Deputy Director of the National Science Foundation Future Renewable Electric Energy Delivery and Management Systems Engineering Research Center, North Carolina State University. His research interests include design and control of power electronic converters and electromagnetic energy conversion with application to microgrids, wireless power transfer, energy storage systems, and electric automotive systems.

Dr. Lukic was a Distinguished Lecturer with the IEEE Vehicular Technology Society from 2011 to 2015.